Research Square

Preprints are preliminary reports that have not undergone peer review.
They should not be considered conclusive, used to inform clinical practice,
or referenced by the media as validated information.

Tract-specific regulation of oligodendrocyte precursor cell activation and glial responses shapes myelin repair

Charles Shuaibu
University of Saskatchewan
Malena Anderson
University of Saskatchewan
Mohammad Amin Abdollahi Far
University of Saskatchewan
Ayesha Shakil
University of Saskatchewan
Catherine Beaupre
University of Saskatchewan
Sarah Donkers
University of Saskatchewan
Olamide Adebiyi
olamide.adebiyi@usask.ca

University of Saskatchewan

Research Article

Keywords: lysophosphatidylcholine, demyelination, myelin, fimbria, lateral olfactory tract, oligodendrocytes

Posted Date: July 15th, 2026

DOI: https://doi.org/10.21203/rs.3.rs-9852062/v1

License: This work is licensed under a Creative Commons Attribution 4.0 International License.
Read Full License

Additional Declarations: No competing interests reported.

Abstract

Oligodendrocytes produce myelin, a multilamellar membrane that ensheathes axons and enables rapid, saltatory conduction. Disruption of myelin integrity is a hallmark of several neurological disorders, including multiple sclerosis, yet therapies aimed at promoting remyelination have shown limited efficacy in clinical trials. A key challenge is that demyelination and repair processes are not uniform across the central nervous system, with different white matter tracts exhibiting distinct vulnerabilities and regenerative capacities. However, the extent to which regional microenvironmental factors and cellular dynamics shape these differences remains incompletely understood.

Here, we used focal lysophosphatidylcholine (LPC)-induced demyelination to compare the spatial and temporal progression of myelin loss and repair in two anatomically and functionally distinct white matter tracts: the hippocampal fimbria and lateral olfactory tract (LOT). Stereotaxic LPC injections were performed in mice, with contralateral saline-injected tracts serving as within-subject controls. Animals were euthanized at multiple times (3, 7, 14, 21 and 28 days post-injection, dpi). Histological and immunohistochemical approaches were employed to quantify lesion evolution, oligodendrocyte lineage dynamics, myelin integrity, glial activation, extracellular matrix, apoptosis, and neuronal density.

We showed that while both tracts eventually showed complete lesion resolution by 28 dpi, the course of demyelination and repair is highly region dependent. The fimbria displays larger lesion diameter and a more rapid recruitment of oligodendrocyte precursor cells, whereas the LOT exhibits an earlier loss of myelin basic protein expression. Despite these differences, both regions follow a coordinated but temporally altered sequence of microglial activation, OPC migration, astroglial response, and extracellular matrix remodeling. Notably, microglial response is consistently lower in the LOT, and the fimbria shows a more prominent expression of the chondroitin sulfate proteoglycan, versican. Apoptosis is transient and neuronal density is preserved in both regions, suggesting that minimal neurodegeneration accompanies LPC-induced demyelination.

Together, these findings demonstrate that LPC-induced demyelination elicits a spatially heterogeneous repair progression shaped by local microenvironmental context. This study highlights regional anatomical variations as contributors to remyelination dynamics and underscores the need for region-tailored approaches to enhance myelin repair.

INTRODUCTION

Myelin is a modified multilayer cellular membrane produced by mature oligodendrocytes (OLs) that ensheathes neuronal axons in the CNS (Emery 2010; López-Muguruza and Matute 2023; Osso and Hughes 2024; Simons and Nave 2015). Damage to myelin and dysfunction of OL lineage cells, coupled with ineffective remyelination, are defining pathological features of neurological disorders such as multiple sclerosis (MS) (Duncan and Radcliff 2016; Garton et al. 2024; Molina_Gonzalez et al. 2022). MS is characterized by chronic inflammation resulting in demyelination and axonal injury, subsequently leading to neurodegeneration and progressive disability (Bebo et al. 2022; Boutitah-Benyaich et al. 2025;

Reich et al. 2018). MS affects about 3 million people globally, and it is the most common non-traumatic neurological disorder among young adults. There is currently no cure, as current therapy only slows down progression. One limitation of effective therapy is the multifaceted nature of the disease, making it difficult to develop a single animal model that fully recapitulates disease features in humans. (Desai et al. 2016; Höftberger and Lassmann 2017). Additionally, much of the available human data is derived from postmortem tissue, which provides only a static endpoint investigation of lesion pathology. Furthermore, *in vivo* experimental studies in preclinical models have predominantly focused on limited brain regions (Oost et al. 2025; Vanderdonckt et al. 2022) despite evidence of distinct susceptibility to demyelination and varying capacities for repair (Rokach et al. 2026; Samtani et al. 2023; Steelman et al. 2012) in multiple brain regions. Thus, our understanding of the spatial and temporal dynamics of demyelination and remyelination that could be valuable in understanding novel therapy remains incomplete.

Hence, the present study aims to address these gaps by characterizing the dynamic progression of lesion formation and repair across prominent yet underexplored white matter tracts using a focal toxin-induced model of demyelination, lysophosphatidylcholine (LPC), to better investigate the progression of evolving lesions across white matter tracts in different brain regions, as seen in clinical disease.

The hippocampal fimbria is a major white matter structure comprising a dense bundle of myelinated axons that emerge from the hippocampus and converge into the fornix, forming a pathway for hippocampal connectivity (Concha et al. 2010; Dogan et al. 2022; Senova et al. 2020; Wyss et al. 1980). It contains both intra- and interhemispheric projections, including fibers that link the two hippocampi via the hippocampal commissure, as well as extensive efferent and afferent connections with subcortical regions such as the hypothalamus and mammillary bodies. In addition, the fimbria contains projections from hippocampal pyramidal neurons alongside cholinergic and non-cholinergic inputs from the basal forebrain, including the medial septum and diagonal band of Broca, arranged in an organized manner across its extent. This convergence of diverse fiber populations underscores the fimbria's role as an integrative tract within hippocampal and limbic circuitry (Wyss et al. 1980). It is enriched in extracellular matrix (ECM) components such as brevican, phosphacan, hyaluronan, and tenascin-R associated with myelinated fiber tract stabilization (Ogawa et al., 2001; Rexrode et al., 2024) suggesting a structured extracellular environment that may influence regenerative responses following injury.

On the other hand, the lateral olfactory tract (LOT) is a highly myelinated white matter tract that exclusively carries olfactory information from the olfactory bulb to olfactory cortices (Lohman and Mentink 1969). Located along the ventrolateral surface of the telencephalon, it is formed by the axons of early-generated mitral and tufted cells, which arise from the olfactory bulb around embryonic day 12 in the mouse and rapidly merge to establish the primary tract (Blanchart et al. 2006; Brunjes et al. 2014). Subsequent development is characterized by the extension of collateral branches along a rostrocaudal gradient, innervating key olfactory regions including the anterior olfactory nucleus, piriform cortex, entorhinal cortex, olfactory tubercle, and amygdala nuclei (Hirata and Frujisawa 1999; Schwob and Price 1984; Soussi-Yanicostas et al. 2002). These projections constitute the main pathway through which

olfactory bulb output is distributed across olfactory networks, underscoring the LOT's central role in integrating sensory processing with limbic and cognitive circuits. Despite its structural and functional importance, the LOT remains underexplored in the context of demyelinating disease. Olfactory dysfunction affects approximately 27% of individuals with MS (Mirmosayyeb et al. 2022; Printza et al. 2022) and it is increasingly recognized as a predictor of more severe disease progression and poorer clinical outcomes (Berek et al. 2024). Notably, postmortem analyses indicate that up to 70% of MS brains exhibit demyelination within the olfactory system (DeLuca et al. 2015), yet the underlying mechanisms and spatiotemporal dynamics of myelin loss in this pathway remain poorly defined.

Given the high degree of myelination within both the fimbria and the LOT, they represent complementary yet underexplored white matter tracts that support distinct but interconnected domains of brain function (memory and sensory processing). Here, we investigate the progression of myelin loss and repair across these tracts, elucidate regional differences in remyelination efficiency and how this is influenced by variations in the local microenvironment, including extracellular matrix, and neuroinflammatory cells, that regulate oligodendrocytes, proliferation, recruitment and maturation.

MATERIAL AND METHODS

Experimental mice

C57BL/6Ncrl mice (Strain #027, 7–8 weeks old, 20–30 g) of both sexes were obtained from Charles River Labs. All animal procedures were approved (#202400093) by the Institutional Animal Research Ethics Board and conducted in accordance with the Canadian Council on Animal Care guidelines. Mice were housed in a controlled environment under standard laboratory conditions (12h light/dark cycle, 50–60% relative humidity), with food and water provided ad libitum. All experimental procedures adhered to the principles of the 3Rs (and were housed under optimal conditions:12h-light/dark cycle, 50–60% relative humidity, with food and water provided *ad libitum*.

Stereotaxic injection of lysophosphatidylcholine

Stereotaxic surgery for intracranial injection of LPC was performed according to published protocols (Athos and Storm 2001; Cecyn and Abrahao 2023; Gabrielli et al. 2022). Briefly, mice received analgesia (meloxicam, 0.1 mg/kg, SC) before surgery. After deep anesthesia with isoflurane (4–5%), a local anesthetic (bupivacaine, 0.01 mg/kg, SC) was administered along the midline of the skull. A midline incision was made to expose the skull, and the Bregma and Lambda were aligned to ensure the skull was level. A small craniotomy was performed using a drill over the targeted region of interest using coordinates relative to Bregma (Hippocampal fimbria: AP: -1.2 mm ML: ±1.0 mm DV: -2.3 mm, LOT: AP: +1.2 mm ML: ±2.0 mm DV: − 2.5 mm) based on the mouse brain atlas (Paxinos and Keith 2019). For each mouse, bilateral injections were performed in both the lateral olfactory tract and the hippocampal fimbria. In the ipsilateral hemisphere, LPC (0.1%, 2000 nl) was injected into both tracts to induce focal

demyelination. The corresponding contralateral tracts were injected with an equivalent volume of saline (0.9% NaCl) and served as within-animal controls, thereby accounting for injection-related effects and inter-animal variability. The injection rate was 8.33 nl/s, and the needle was left in place for 4 minutes before slow withdrawal to minimize backflow. Incisions were closed with sutures, and animals were returned to clean cages and monitored postoperatively.

Euthanasia

To track cellular events, mice were euthanized multiple times (3-, 7-, 14-, 21-, and 28-, day post-injection, **(Fig. 1A**). At each time point, a cohort of mice (n = 4; 2 males, 2 females, total of 20 across all timepoints) was deeply anesthetized with tribromoethanol (600 mg/kg, intraperitoneally) and intracardially perfused with ice-cold PBS followed by 4% paraformaldehyde (PFA) in PBS. Brains were dissected and post-fixed in 4% PFA for 24 hours, then cryoprotected in 30% sucrose at 4°C for 48 hours. Brains were subsequently embedded in optimal cutting temperature (OCT) medium and stored at -80°C. Coronal sections (20 µm) were cut using a Leica cryostat (CM 1850, Germany), and the region of interest was examined.

Immunohistochemistry

Brain sections were permeabilized with 1X PBS containing 0.3% Triton X-100 for 20 minutes and then washed three times for 10 minutes each. If epitope retrieval was necessary, tissue samples were incubated in saline citrate buffer solution for 30 minutes at 90 ^{0}C. The tissue was allowed to cool at room temperature before washing in PBS for five minutes, three times. The sections were then incubated for one hour in a quenching solution (glycine and 0.25% Triton X-100 in PBS). Sections were washed again, three washes of five minutes each. Slides were taken out of the PBS, carefully dried, and sections were outlined with a hydrophobic pen. The sections were incubated in blocking solution (5% bovine serum albumin, 2% normal goat serum), and 0.1% Triton X-100 in 1x PBS for 1 hr at room temperature. Primary antibodies were applied overnight at 4 ^{0}C. The tissue sections were washed in 1X PBS for 10 minutes, three times, and incubated with fluorophore-conjugated secondary antibodies for 1 hour at room temperature. A list of primary and secondary antibodies used is presented in the additional data (Table 1**)**. Following incubation, the sections were washed again in 1X PBS for 10 minutes, three times, and mounted onto glass slides using ProLong Gold antifade mounting medium containing DAPI. Images were acquired using an inverted widefield fluorescence microscope (Olympus IX83). A 20×/0.45 objective lens (NA: 0.4–0.75) was used for all image acquisition. Imaging was performed at room temperature (~ 22–25°C). Images were captured using an Olympus DP73 and acquired with Olympus cellSens software and images were exported in TIFF format.

Table 1
List of primary antibodies used

Antibody	Catalog number	Company	Host	Dilution factor
Anti-Iba1	Ab178846	Abcam	Rabbit	1:1000
Anti-GFAP	ab4674	Abcam	Chicken	1:500
MBP polyclonal	PA5-78397	Invitrogen	Rabbit	1:500
PDGFR-α monoclonal	ab90967	Abcam	Rat	1:200
Olig-2 polyclonal	PA5-85734	Invitrogen	Rabbit	1:1000
Brevican Monoclonal	75–281	Invitrogen	Mouse	1:100
Versican Polyclonal	bs-2533R	Invitrogen	Rat	1:200
Caspase 3 Monoclonal	66470-2-Ig	Proteintech	Mouse	1:500
NeuN Polyclonal	PA5-143567	Invitrogen	Chicken	1:5000

Image analysis and cell counting

Immunohistochemical quantification was conducted using ImageJ software (Fiji). The number of positive cells was quantified within predefined regions of interest (ROIs) encompassing the lesion area, and the data were expressed as the percentage area occupied within the lesion site. Furthermore, the intensity of MBP expression images was quantified by measuring the mean gray value after background subtraction using identical threshold settings for all images. Microglial morphology was identified as previously described (Schwabenland et al., 2021; Green and Rowe, 2024). Briefly, ramified: small cell bodies with long, highly branched processes; hypertrophic: large cell bodies with shorter, thicker processes; amoeboid: round cell bodies with almost no process; rod-like: elongated cell bodies with processes lined up in one direction. All microglial measurements and shape analyses were performed using the ImageJ AnalyzeSkeleton and FracLac plugins. Colocalization analysis was performed using the ImageJ JACop plugin, and colocalization was quantified using Pearson's correlation coefficient and Manders' overlap coefficient within predefined ROIs. To measure the lesion diameter, the image scale was calibrated by assigning 1000 pixels to 270.83 μm, allowing all subsequent measurements to be expressed in micrometers according to methods described by Schneider et al. (2012). Lesion boundaries within the LPC/saline-injected regions of the LOT and hippocampal fimbria were delineated using the polygon selection tool to define the region of interest. To quantify the lesion diameter, a linear measurement was then made by calculating the maximum distance between opposing margins of the delineated area. Cell counting was done blindly to minimize experimenter bias.

Statistical analysis

Statistical analyses were performed using GraphPad Prism 10.4.2. Data normality was confirmed by using the Shapiro-Wilk's test before analysis, and all datasets were analyzed without transformation. Homogeneity of variance was evaluated using Levene's test. Experimental animals were randomly assigned to one of five post-operative time points, with four mice per time point (total n = 20). Statistical analyses were performed using a two-way mixed-effects analysis of variance (ANOVA), with time (five timepoints; between-subject factor) and treatment (LPC vs saline; within-subject factor). Tukey's post-hoc test was used for multiple comparisons. Data are presented as mean ± standard deviation (SD), and statistical significance was set at $\alpha = 0.05$, with exact p-values reported where applicable.

RESULTS

LPC induces slightly larger lesion diameters in the fimbria than in the LOT, despite similar resolution patterns

To quantify the extent of damage to brain tissue, assess lesion evolution and resolution, we measured lesion diameter in the fimbria and LOT (**Fig. 1B**). The lesion area gradually decreased from 3 to 28 days post-injection (DPI) in both white matter tracts. Although the saline and LPC injection sites showed a progressive reduction in lesion diameter over time, the ipsilateral LPC site consistently exhibited a slightly larger lesion diameter at every time points (**Fig. 1C, D**). Additionally, although both tracts exhibited similar reductions in lesion size, the fimbria ipsilateral lesion site consistently showed a greater lesion diameter across all time points.

Figure 1. Lysophosphatidylcholine (LPC)-induced demyelination of the hippocampal fimbria (HPF) and lateral olfactory tract (LOT). (**A**) Timeline indicating the experimental design and intracranial injection of LPC (ipsilateral hemisphere) and saline (contralateral hemisphere) in the HPF and LOT and subsequent euthanasia and analysis at 3, 7-, 14-, 21- and 28 days post-injection (dpi). (**B**) Representative images for IBA immunofluorescent staining showing lesion site in the fimbria and LOT following the injection of LPC. Scale bar, 20 µm. Yellow line indicates the lesion diameter. Data analysis of lesion diameter in the (**C**) fimbria and (**D**) LOT regions at different time points (3–28 dpi). Data is presented as mean ± SD, and statistical analysis was conducted using two-way mixed-effects ANOVA by Tukey's multiple comparisons test (n = 20). The red and blue squares show injection site in the ipsilateral and contralateral hemisphere, respectively.

OPC recruitment precedes spontaneous myelin repair following LPC-induced demyelination

Given the role of Olig2 in oligodendrocyte lineage progression, we hypothesized that LPC-induced demyelination disrupts its expression across the stages of oligodendrocyte development. We therefore assessed Olig2 expression in oligodendrocyte precursor cells (OPCs) by co-staining with PDGFRα in the hippocampal fimbria and LOT (**Fig. 2, 3**). In the fimbria, $Olig2^+$ cell density was significantly reduced at the ipsilateral LPC lesion sites at 3 and 7 dpi ($p = 0.0115$ and $p < 0.0001$ respectively), whereas levels

were comparable to the contralateral saline site at later time points (**Fig. 2B**). In contrast, PDGFRα⁺ OPC density was significantly increased at the LPC lesion site as early as 3 dpi ($p = 0.0193$) and peaked at 7 dpi ($p = 0.0053$), before declining thereafter. Although PDGFRα⁺ levels were similar between LPC and saline sites from 14 to 28 DPI, densities at 21 and 28 DPI were significantly lower than those observed at 3 and 7 dpi within the lesion **site (Fig. 2C).** PDGFRα⁺ OPCs were confirmed by co-localization of PDGFRα immunoreactivity with Olig2-positive nuclei. (**Fig. 2C, 3C**).

In the LOT, Olig2 expression exhibited a temporal pattern like that observed in the hippocampal fimbria. Olig2⁺ cells increased steadily over time in both LPC- and saline-injected sites; however, densities were significantly reduced at the LPC lesion site at 3 and 7 dpi compared to 28 dpi ($p = 0.03$ and $p < 0.001$ respectively, **Fig. 3B**). Consistent with findings in the fimbriae, PDGFRα⁺ OPCs were significantly higher at the LPC lesion site relative to the contralateral saline site but not until at 7 dpi ($p = 0.053$) and remained elevated at subsequent time points (**Fig. 3C**). However, analysis of the ipsilateral LPC lesion site demonstrated a significant reduction in PDGFRα⁺ OPCs at 14–28 dpi compared with earlier time points.

Figure 2. Oligodendrocyte precursor cell recruitment and Olig2 lineage progression in fimbrial lesion site (**A**) Representative images of Olig2 (green) and PDGFRα (red) double immunofluorescence staining in the fimbria at 3, 7, 14, 21, and 28 days post-injury (dpi) following injection of LPC and saline Scale bar: 50 μm. The white square inset images show a higher magnification of the region surrounding the injection sites. Scale bar: 20 μm. Quantification of (**B**) Olig2⁺ cells, (**C**) PDGFRα⁺ cells, and (**D**) Olig2⁺ and PDGFRα⁺ co-localized cells within the lesion site in the fimbria across different time points (3–28 dpi). Data is presented as mean ± SD. Statistical analysis was performed using two-way mixed-effects ANOVA followed by Tukey's multiple comparisons test to assess differences across time points and within the lesion site. (n = 20). Exact *p* values are indicated in the graphs.

Figure 3. Oligodendrocyte precursor cell recruitment and Olig2 lineage progression in the lateral olfactory tract (LOT) lesion site (**A**) Representative images of Olig2 (green) and PDGFRα (red) double immunofluorescence staining in the LOT during the post-injury time course (3–28 dpi) following injection of LPC and saline. Scale bar: 50 μm. The white square inset images show a higher magnification of the region surrounding the injection sites. Scale bar: 20 μm. Quantification of (**B**) Olig2⁺ cells, (**C**) PDGFRα⁺ cells, and (**D**) Olig2⁺ and PDGFRα⁺ co-localized cells within the lesion site in the LOT across different time points (3–28 dpi). Data is presented as mean ± SD. Statistical analysis was performed using two-way mixed-effects ANOVA followed by Tukey's multiple comparisons test to assess differences across time points and within the lesion site. Exact *p* values are indicated in the graphs.

Myelin loss is accompanied by apoptotic neuronal cell death

Following the apparent inverse relationship between Olig2 expression and PDGFRα⁺ OPCs levels, we next investigated whether the reduced Olig2 levels reflected altered levels of other oligodendroglial lineage cells. To address this, we quantified myelin basic protein (MBP) expression, a marker of mature

oligodendrocytes. In parallel, we assessed neuronal survival following LPC-induced demyelination by co-staining for NeuN and cleaved caspase-3 (casp3) **(Fig. 4, 5).** In the fimbria, MBP levels were significantly reduced at the LPC lesion site at 7 dpi relative to the saline site, suggesting acute demyelination. However, MBP expression increased thereafter, reaching levels comparable to the saline site between 14 and 28 dpi, significantly exceeding those observed within the ipsilateral lesion site during the early demyelinating timepoints (3–7 dpi). (**Fig. 4B).** A similar but earlier pattern of demyelination was observed in the LOT. MBP expression at the LPC lesion site was significantly reduced as early as 3 dpi and remained decreased at 7 dpi relative to the saline site. By contrast, MBP levels re-established between 14 and 28 dpi, at which time they were comparable between LPC and saline sites and significantly higher within the lesion site than those observed during the early post-lesion time point (**Fig. 5B**).

Despite these transient changes in myelin integrity, neuronal survival was largely preserved following LPC injection. In the fimbria, the overall number of $NeuN^+$ neurons did not differ significantly between LPC and saline sites across time points. However, within the lesion site, $NeuN^+$ cell density was transiently reduced at 3 and 7 dpi compared with later time points (14–28 dpi) (**Fig. 4C**). Assessing apoptotic neuronal death in the fimbria, we found no significant interaction between time and treatment (2-way mixed-effects ANOVA, $F_{(4,30)} = 0.1417$, $p = 0.2515$). In contrast, there were significant main effects of both treatment ($F_{(1,10)} = 12.65$, $p = 0.0052$) and time ($F_{(2,13)} = 22.23$, $p < 0.0001$), indicating that each factor independently influenced neuronal apoptosis. Colocalization of NeuN and caspase peaked at 14 days post-injury (dpi) in the LPC-treated hemisphere (**Fig. 4D**), compared with 7 dpi ($p = 0.003$). By 28 dpi, colocalization was reduced relative to 14 dpi ($p = 0.0035$), but remained significantly elevated compared with 7 dpi ($p = 0.0301$). In contrast, neuronal density in the LOT remained stable across both ipsilateral and contralateral lesion sites and time points, with no detectable differences (**Fig. 5C).**

Figure 4. Extent of demyelination, neuronal density and apoptosis at the fimbrial lesion site (**A**) Representative immunofluorescence images showing MBP (green), NeuN (magenta), and Caspase-3 (red) expression in the fimbria at 3, 7, 14, 21, and 28 days post-injury (dpi), scale bar = 50 μm. The white square inset images show a higher magnification of the region surrounding the injection sites. Scale bar: 20 μm. Quantification of (**B**) Myelin basic protein MBP intensity, (**C**) NeuN and (**D**) Caspase-3 and NeuN colocalization in the fimbrial lesion site across different time points (3–28 dpi). Data is presented as mean ± SD. Statistical analysis was performed using two-way mixed-effects ANOVA followed by Tukey's multiple comparisons test to assess differences across time points and within the lesion site (n = 20). Exact *p* values are indicated in the graphs.

Figure 5. Extent of demyelination, neuronal density and apoptosis at the lateral olfactory tract (LOT) lesion site (**A**) Representative immunofluorescence images showing MBP (green), NeuN (magenta), and Caspase-3 (red) expression in the LOT at 3, 7, 14, 21, and 28 days post-injury (dpi), scale bar = 50 μm. The white square inset images show a higher magnification of the region surrounding the injection sites. Scale bar: 20 μm. Quantification of (**B**) Myelin basic protein MBP intensity, (**C**) NeuN and (**D**) Caspase-3 and NeuN colocalization within the LOT lesion site across different time points (3–28 dpi). Data is

presented as mean ± SD. Statistical analysis was performed using two-way mixed-effects ANOVA followed by Tukey's multiple comparisons test to assess differences across time points and within the lesion site (n = 20). Exact *p* values are indicated in the graphs.

Reactive gliosis peaks at 7 DPI and resolves by 21 DPI in the hippocampal fimbriae and LOT

In the hippocampal fimbriae, IBA1-positive microglial density was significantly higher at the ipsilateral LPC injection site than at the contralateral saline site at 3 to 14 dpi ($p < 0.0001$). Microglial density peaked at 7 dpi and declined from 14 to 28 dpi. The difference between the ipsilateral and contralateral sites was significant at 3, 7, and 14 dpi ($p = 0.0004$, $p < 0.0001$, and $p < 0.001$, respectively), but by 21 and 28 dpi microglial densities were similar between the two sites. Within the LPC-injected ipsilateral sites, IBA1-positive microglial density also varied significantly across time points. Densities at 7 dpi were significantly higher than those at all other time points. Densities at 3 and 14 dpi were comparable to each other but lower than those at 7 dpi and higher than those observed at 21 and 28 dpi (**Fig. 6A, B**).

Given the pronounced acute increase in microglial density, we next characterized and quantified microglial morphology at time points showing significant changes (3, 7, and 14 dpi, **Additional Fig. 2A**). Two-way mixed-effects ANOVA revealed a significant interaction between time and treatment ($F_{(4,56)} = 5.850$). At 3 dpi, microglia predominantly exhibited an amoeboid morphology at both sites; however, quantitative analysis revealed no significant difference between the ipsilateral LPC lesion and the contralateral saline site. The density of amoeboid microglia declined significantly at subsequent time points ($p < 0.001$) and was no longer detectable by 21 dpi (**Additional Fig. 2C).** At 7 dpi, hypertrophic microglia, characterized by enlarged cell bodies and thickened processes, became the predominant phenotype; their density subsequently declined at later time points (**Additional Fig. 2D**). Rod-like microglia were not observed at 3 DPI but appeared at 7 dpi, reaching peak density at 14 dpi. At this time, their density was significantly higher in the ipsilateral LPC lesion than in the contralateral saline site ($p = 0.0115$), before declining at 21 and 28 dpi (**Additional Fig. 2E**). By 21 and 28 dpi, microglia progressively transitioned toward a ramified morphology with similar densities (**Additional Fig. 2F**).

Next, astrocytic activation, assessed by GFAP immunoreactivity, revealed a peak at the LPC lesion site at 7 dpi ($p < 0.001$) and declined between 14 and 28 dpi. GFAP levels were significantly higher at the ipsilateral LPC site than at the contralateral saline site at 3 and 7 dpi ($p = 0.0020$ and $p = 0.0073$, respectively) but did not differ between sites from 14 to 28 DPI (**Fig. 6C**).

In the LOT, the microglial population exhibited a temporal pattern of IBA1-positive cells like that observed in the fimbria across all time points (**Fig. 7A**). However, total IBA1 expression at the LPC lesion site was consistently lower in the LOT than in the hippocampal fimbria (**Fig. 7B**). Microglial morphological phenotypes also followed comparable temporal changes in the LOT (**Additional Fig. 2G-J**). Nonetheless, hypertrophic microglial density at the LPC lesion site in the LOT was significantly higher than at the contralateral saline site at 7 and 14 dpi, whereas densities at these time points were similar between sites in the hippocampal fimbriae. Rod-like microglia also appeared later in the LOT, beginning at 14 dpi compared with 7 dpi in the hippocampal fimbria. Consistent with the fimbria, $GFAP^+$ cell expression

progressively increased at the ipsilateral site; however, in the LOT, elevated levels persisted until 14 dpi (**Fig. 7C**).

Figure 6. Astrocyte and microglial response at the fimbrial lesion site (**A**) Representative immunofluorescence images showing microglial (green) and astrocyte (magenta) accumulation at the lesion site in the fimbria at 3, 7, 14, 21, and 28 days post-injury (dpi). Scale bar: 50 μm. The white square inset images show a higher magnification of the region surrounding the injection sites. Scale bar: 20 μm. (**B**) Quantification of IBA-1 positive microglial and (**C**) GFAP positive astrocytes in the fimbria across different time points (3–28 dpi). Data is presented as mean ± SD. Statistical analysis was performed using two-way mixed-effects ANOVA followed by Tukey's multiple comparisons test to assess differences across time points and within the lesion site (n = 20). Exact *p* values are indicated in the graphs.

Figure 7. Astrocyte and microglial response at the lateral olfactory tract (LOT) lesion site (**A**) Representative immunofluorescence images showing microglial (green) and astrocyte (magenta) accumulation at the LOT at 3, 7, 14, 21, and 28 days post-injury (dpi). Scale bar: 50 μm. The white square inset images show a higher magnification of the region surrounding the injection sites. Scale bar: 20 μm. (**B**) Quantification of IBA-1 positive microglial and (**C**) GFAP positive astrocytes in the LOT across different time points (3–28 dpi). Data is presented as mean ± SD. Statistical analysis was performed using two-way mixed-effects ANOVA followed by Tukey's multiple comparisons test to assess differences across time points and within the lesion site (n = 20). Exact *p* values are indicated in the graphs.

Extracellular matrix remodeling in the fimbria and LOT

To investigate how extracellular matrix remodeling relates to the timing of myelin repair, we examined the chondroitin sulfate proteoglycans brevican and versican, key components of the inhibitory extracellular matrix in the injured CNS. We quantified their expression across time points and assessed whether changes in their levels coincide with alterations in oligodendrocyte lineage cells and myelin repair **(Additional Fig. 2**). Their expressions were similar between the ipsilateral and contralateral lesion sites across all time points (**Additional Fig. 2B, C**). However, lesion site–specific analysis revealed distinct temporal dynamics: versican expression peaked at 7 dpi before gradually declining from 14 to 28 dpi, whereas brevican expression showed a delayed increase, reaching significantly higher levels at 28 dpi.

In the LOT, versican expression exhibited a pronounced, time-dependent increase at both LPC and saline injection sites. Specifically, versican$^+$ cell density increased significantly at early time points, reaching a peak at 7 dpi. This early elevation was followed by a progressive decline from 14 through 28 dpi, with levels approaching baseline by the later stages. Brevican expression exhibited a delayed but sustained increase following LPC-induced demyelination in the LOT. In contrast to versican, brevican$^+$ cell density did not show a pronounced early peak but remained relatively stable at initial time points. A significant elevation emerged at later stages, with levels at 28 dpi markedly higher than at earlier time points.

DISCUSSION

The complex and multifocal nature of demyelinating lesions in multiple sclerosis (MS) presents a significant challenge for understanding the cellular, inflammatory, and myelin-specific processes that underline lesion evolution and repair (Boutitah-Benyaich et al. 2025; Tafti et al. 2026). Particularly challenging is that lesions arise across diverse white matter tracts and anatomical regions, each characterized by distinct microenvironments and immune responses, thus complicating efforts to study discrete mechanisms in isolation. To address this, we employed the lysophosphatidylcholine (LPC) toxin-induced demyelination model, which is widely used for its ability to produce focal lesions with a highly reproducible course of demyelination and remyelination (Peruzzotti-Jametti et al. 2025; Plemel et al. 2018; Vereyken et al. 2009; Yamazaki et al. 2021).

We observed region-specific differences in lesion progression measured by lesion diameter across both tracts, indicating heterogeneity in LPC-induced lesions. Such disparity in lesion evolution has been reported in focal demyelination models, reflecting distinct patterns of cellular response and anatomical location depending on local microenvironment factors (Blakemore and Franklin 2008). This parallels the report by Serwanski et al. (2018), that observed that differential recruitment and OPCs differentiation influence the timing and extent of lesion progression in the corpus callosum, with local OPCs rapidly proliferating and generating OLs within LPC lesions, while more distal neural stem cells contribute to repopulating OPC pools at later times. These findings suggest that tract-specific microenvironments influence temporal dynamics of demyelination and remyelination, resulting in region-dependent differences in lesion evolution across white matter tracts. Accordingly, this suggests that, despite the widespread use of LPC as a demyelinating model, studies should evaluate lesions within a region-specific context.

Platelet-derived factor receptor, PDGFRα is upregulated at lesion site to drive precursor cell proliferation following LPC-induced demyelination. These findings support PDGFRα activation as an early response to demyelinating injury, consistent with its role in driving precursor proliferation during the initial phase of repair. This observation is in consonance with previous reports identifying PDGFRα$^+$ OPCs as the proliferative population across multiple CNS regions following focal demyelination, including the forebrain, medulla and spinal cord (Hiratsuka et al. 2019; Kataria et al. 2018; Redwine and Armstrong 1998). Genetic studies further support a causal role for PDGFRα signaling in this process. Conditional ablation of PDGFRα specifically in OPCs significantly impairs their proliferative abilities highlighting the importance of this pathway for efficient remyelination (Zhu at al. 2014). In parallel, transcriptomic analyses of OPCs isolated from demyelinated lesions reveal enrichment of PDGF-responsive gene networks, (Baydyuk et al, 2020), suggesting that PDGFRα activation is part of a broader injury-induced transcriptional program that primes these cells for cell cycle entry.

Notably, the present study demonstrates a regional distinction in PDGFRα dynamics, with an earlier and pronounced increase observed in the fimbria relative to the LOT. This suggests that white matter tracts differ in their temporal responsiveness to demyelination, The more rapid onset of OPC proliferation in the

fimbria could reflect its unique anatomical positioning adjacent to the subventricular zone (SVZ), which provides a readily available reservoir of progenitors capable of rapid mobilization (Azim et al. 2012). While heterogeneity in OPC proliferation across grey and white matter has been previously reported (Young et al. 2013), the present data expands these findings demonstrating a within-white matter tract differences in PDGFRα activation, highlighting a spatial regulation in the remyelination response. The temporal profile observed here, characterized by an early increase followed by a reduction in PDGFRα density by 14 dpi, further supports a time-specific role for PDGFRα signaling. While activation of this pathway promotes OPC proliferation, its downregulation appears necessary for subsequent differentiation and remyelination. Indeed, prolonged PDGFRα signaling has been shown to maintain OPCs in a progenitor state and delay myelin gene expression (Calver et al. 1998), suggesting that the decline in PDGFRα expression observed at the later time points in our study may reflect a transition from proliferation to differentiation within the lesion environment to enhance myelin repair.

Furthermore, the temporal increase in PDGFRα observed in both the fimbria and LOT corresponds to marked reduction in MBP, a membrane protein localized at the cytoplasmic surface of mature oligodendrocyte, that is critical for myelin compaction (Bijlard et al. 2016), consistent with an acute toxin-mediated myelin loss induced by LPC. This inverse relationship between PDGFRα expression and MBP levels is in line with previous studies demonstrating that LPC-induced demyelination leads to rapid mature oligodendrocyte loss and myelin breakdown, followed by a compensatory elevation of OPCs within the lesion site (Baaklini et al. 2023; Keough et al. 2016). Additionally, studies demonstrated that PDGFRα and MBP are not co-expressed by oligodendrocytes at any stage of differentiation (Zhu et al. 2014; Butt et al. 1997; Zheng et al. 2018). Our findings support this hypothesis, going by the temporal dynamics with PDGFRα expression reduction before MBP expression increase indicating a sequential rather than simultaneous pattern. The decreased MBP expression at early points in both fimbria and LOT is consistent with an acute loss of myelin induced by the toxin, LPC. The more rapid onset of demyelination in the LOT may be due to relatively distant location of the LOT from the SVZ, an established source of OPCs, in comparison to the fimbria. The early phase loss of myelin in both tracts is explained by the lipid-disrupting properties of lysolecithin. Remarkably, despite the initial regional differences in the extent and kinetics of demyelination, the restoration of MBP to baseline in both tracts by 21 dpi highlights the self-limiting nature of LPC-induced toxicity. Additionally, the period of minimal MBP expression (7 dpi) was accompanied by peak microglial activation. Following this peak, microglial accumulation within the lesion sites declined to near baseline levels by 21 dpi, indicative of a transient, acute neuroinflammatory response characterized by glial activation (Kraft and Jean Harry 2011) and the role of microglia in clearing myelin debris (Lloyd and Miron 2019). The initial microglial phenotypes at day 3–7 dpi indicate pro-inflammatory response that have been linked to the requisite response needed to activate OPC proliferation and survival, while the upregulation of the anti-inflammatory phenotype that occurs later during lesion evolution is important to generate the factors for OPC differentiation (Miron et al. 2013). This distinct correlation between microglial infiltration and OPC recruitment suggests that the inflammatory response observed in demyelination may be a requirement for oligodendrocyte regeneration (Glezer et al. 2007; Shigemoto-Mogami et al. 2014). Although both tracts exhibited a similar

temporal pattern, evident by an early increase in microglial activation followed by a mid-to-late-phase resolution, a striking finding was the heightened microglial response observed in the fimbria at 28 dpi. This suggests a relatively sustained microglial activity in the fimbria compared to the LOT. One possible explanation relates to tract-specific structural and anatomical properties. The fimbria, being the largest output pathway of the hippocampus, constitutes a substantially larger and more densely organized white matter tract than the LOT (Senova et al. 2020). Its greater volume and surface area may necessitate increased microglial recruitment and prolong the clearance process. Additionally, the deeply located dense afferent fibers within the fimbria likely correspond to a higher oligodendrocyte population, leading to greater accumulation of myelin debris secondary to LPC-induced toxicity (Stidworthy et al. 2006). Taken together, with the findings that the fimbria exhibited larger lesion areas, this underscores that regional differences in axonal architecture is a major contributing factor to the rate of lesion resolution

The neuronal population was preserved in the LOT throughout the tracked timeline. Temporal trends, however, revealed an early phase decline in the neuronal population of fimbria at 3 and 7 dpi, which was found to be statistically significant in comparison to 28 dpi. The significant neuronal vulnerability observed in the fimbria in the early to mid-timepoints post-injection could reflect a pronounced sensitivity of white-matter tracts to transient demyelination. This sensitivity has been linked to axonal stress in previous studies (Irvine and Blakemore 2008). Our results revealed a synchronized peak in apoptotic neuronal loss in both the LOT and the fimbria at 14 dpi, corresponding with the window of maximal oligodendroglial lineage loss. Notably, the fimbria exhibited sustained apoptotic activity, which persisted into 14 dpi, unlike the LOT which demonstrated a more rapid return to saline levels. The resolution of apoptotic activity in both tracts by 21 dpi, marked by a return to saline levels, coincide with the window of repair and oligodendrocyte regeneration. Apoptotic signaling was largely restricted to early post-injury timepoints across regions. This pattern is consistent with studies demonstrating that LPC acts primarily as a lipid-disrupting agent that induces rapid but transient cellular injury, sparing axons and neurons once the toxin is cleared (Plemel et al. 2018).

Temporal profiling of the lesion microenvironment revealed region-specific dynamics in versican-associated extracellular matrix (ECM) remodeling. Although both tracts followed a broadly similar trajectory over time, the fimbria exhibited a more pronounced and rapid early response, consistent with increased sensitivity to injury-induced changes in matrix composition. In contrast, the LOT showed a more limited profile, suggesting differential regulation of extracellular matrix turnover across white matter tracts. The loss of versican has been associated with ongoing cell death in previous studies (Kenagy et al. 2009) but the temporal dynamics in the LOT and the fimbria suggest a different trajectory. Rather than reflecting a uniform association with degeneration, versican dynamics may instead capture distinct phases of microenvironmental adaptation, including transient matrix expansion and subsequent resolution. Given that versican is known to be a product of differentiating OPCs but is downregulated during terminal differentiation, the late phase decline suggests a successful differentiation of OPCs into mature oligodendrocytes capable of myelination (Asher et al. 2002). This is supported by our observation of a late-phase restoration of MBP observed in both tracts. This elevation was sustained with the mean area covered remaining relatively stable throughout the 28 dpi. In the fimbria, the mean

expression remained relatively stable in the early to mid-time-points. However, at 28 dpi, a late phase surge which was significant in comparison to the earlier timepoints was observed. The significant late-phase increase of Brevican^{+} cells in the fimbria points towards a robust reestablishment of the structural ECM following remyelination (Harlow and Macklin 2014). While chondroitin sulfate glycoproteins like versican are associated with an inhibition of repair, brevican has been demonstrated to promote the maturation and proliferation of mature myelinating oligodendrocytes, in addition to establishing perineuronal nets and the nodes of Ranvier (Bekku et al. 2009; Ghorbani et al. 2022). The significant late-phase reduction in versican-positive cells observed in the LOT and sustained expression of Brevican observed in the fimbria point towards spatial distinct constraints on remyelination consistent with region-specific effects of chondroitin sulfate proteoglycans (Keough et al. 2016) .

Together, these findings support that PDGFRα activation constitutes an early, regionally heterogeneous response to demyelination that drives OPC proliferation, and is tightly regulated to promote remyelination. We report a peak demyelination in both fimbria and LOT at 7dpi, this timeline aligns with observations in the internal capsule reported by Yamazaki et al. (2023) but differs from findings by Plemel et al. (2018), who observed peak demyelination as early as 24 hours following LPC injection in the ventral column of the spinal cord. These incongruences underscore an important point, although LPC reliably induces demyelination across multiple white matter tracts, the temporal dynamics of myelin loss are highly tract specific. While this study focused on the glial and lesion microenvironment driven mechanisms of repair, we acknowledge that the innate immune response, a significant contributor to the demyelinating microenvironment (Dong and Yong 2019) is a possible source of physiological variance. Although we utilized within-animal contralateral injections to provide an internal baseline control to mitigate this limitation to reduce the impact of inter-animal variability and systemic differences in immune status, thereby strengthening the inference that the observed effects are regionally driven rather than primarily attributable to subject factors. Future studies examining immune profiling will be important to resolve subject differences in inflammatory responses contributions to the observed heterogeneity. A further limitation of this study is the lack of sufficient statistical power to assess sex-specific effects. As this study was designed as an exploratory, descriptive time-course analysis, the aim was to characterize temporal cellular and pathological changes rather than to evaluate sex differences. Consequently, the study was not powered for sex-based comparisons. Although this limits definitive inference regarding sex-specific responses, the observed temporal patterns and treatment-related effects were consistent and provide a strong foundation for future hypothesis-driven studies incorporating formal power calculations and dedicated sex-based analyses.

These findings suggest that LPC induced localized demyelination followed a coordinated but non-uniform lesion resolution in different white matter tract. This regional heterogeneity has important implications for therapeutic strategies, highlighting the need to consider anatomical context as a crucial determinant of regenerative outcome and suggests that strategies to enhance remyelination will need to account for local differences in glial and extracellular matrix signaling.

Additional Fig. 1

Representative immunofluorescence images showing microglia phenotypes prominent at the lesion sites at 3, 7, 14, 21, and 28 days post-injury (dpi). (A) Microglia were labeled with IBA1, and morphological phenotypes were classified and quantified within ipsilateral and contralateral fimbria at 3–28 dpi (**B**) Images were pre-processed in ImageJ prior to analysis and identified as amoeboid, hypertrophied, rod-like and ramified. (**C–F**) Quantification of distinct IBA1$^+$ microglial morphologies in ipsilateral and contralateral fimbria across the post-injury time course (**G-J**) Quantification of distinct IBA1$^+$ microglial morphologies in ipsilateral and contralateral LOT across the post-injury time course. Data is presented as mean ± SD. Statistical analysis was performed using two-way mixed-effects ANOVA followed by Tukey's multiple comparisons test to assess differences across time points and within the lesion site (n = 20). Exact p values are indicated in the graphs.

Additional Fig. 2. Extracellular matrix visualization at the fimbrial lesion site. (**A**) Representative immunofluorescence images showing double labeling for versican (green) and brevican (red) in the fimbria across the post-injury time course (3–28 dpi) following LPC or saline injection. Scale bar: 50 μm. The white square inset images show a higher magnification of the region surrounding the injection sites. Scale bar: 20 μm. Quantification of (**B**) versican and (**C**) brevican expression within the lesion site in the fimbria across different time points (3–28 dpi). Data is presented as mean ± SD. Statistical analysis was performed using two-way mixed-effects ANOVA followed by Tukey's multiple comparisons test to assess differences across time points and within the lesion site (n = 20). Exact p values are indicated in the graphs.

Additional Fig. 3. Extracellular matrix visualization at the lateral olfactory tract (LOT) lesion site (**A**) Representative immunofluorescence images showing double labeling for versican (green) and brevican (red) in the LOT across the post-injury time course (3–28 dpi) following LPC or saline injection. Scale bar: 50 μm. The white square inset images show a higher magnification of the region surrounding the injection sites. Scale bar: 20 μm. Quantification of (**B**) versican and (**C**) brevican expression within the lesion site in the LOT across different time points (3–28 dpi). Data is presented as mean ± SD. Statistical analysis was performed using two-way mixed-effects ANOVA followed by Tukey's multiple comparisons test to assess differences across time points and within the lesion site (n = 20). Exact p values are indicated in the graphs.

Declarations

Ethics approval and consent to participate

The use of animals was approved by our Institutional Animal Research Ethics Board (#20240093) and carried out in accordance with approved guidelines.

Consent for publication

Not applicable.

Competing interests

The authors declare no competing interests.

Funding

This study was supported by the Saskatchewan Health Research Foundation Establishment Grant and Natural Sciences and Engineering Research Council of Canada Discovery Grant to OA.

Author Contribution

C.S., M.A., A.S., M.A.F. and O.A wrote the main manuscript text, C.S., M.A., A.S., M.A.F. data acquisition and analysis, C.S., and M.A.F. prepared the figures, C.B., S.D., and O.A .conception of the work, O.A. study design and funding acquisition. All authors reviewed the manuscript.

Data Availability

The datasets supporting the conclusions of this article are included within the article and its additional files.

References

1. Asher RA, Morgenstern DA, Shearer MC, Adcock KH, Pesheva P, Fawcett JW (2002) Versican Is Upregulated in CNS Injury and Is a Product of Oligodendrocyte Lineage Cells. J Neurosci 22(6):2225–2236. https://doi.org/10.1523/jneurosci.22-06-02225.2002
2. Athos J, Storm DR (2001) High precision stereotaxic surgery in mice. *Current Protocols in Neuroscience / Editorial Board, Jacqueline N. Crawley … et Al.]*, *Appendix 4*(1), A.4A.1-A.4A.9. https://doi.org/10.1002/0471142301.nsa04as14
3. Azim K, Raineteau O, Butt AM (2012) Intraventricular injection of FGF-2 promotes generation of oligodendrocyte-lineage cells in the postnatal and adult forebrain. Glia 60(12):1977–1990. https://doi.org/10.1002/glia.22413
4. Baaklini CS, Ho MFS, Lange T, Hammond BP, Panda SP, Zirngibl M, Zia S, Himmelsbach K, Rana H, Phillips B, Antoszko D, Ibanga J, Lopez M, Lee KV, Keough MB, Caprariello AV, Kerr BJ, Plemel JR (2023) Microglia promote remyelination independent of their role in clearing myelin debris. Cell Rep 42(12). https://doi.org/10.1016/j.celrep.2023.113574
5. Baydyuk M, Morrison VE, Gross PS, Huang JK (2020) Extrinsic Factors Driving Oligodendrocyte Lineage Cell Progression in CNS Development and Injury. Neurochem Res 45(3):630. https://doi.org/10.1007/s11064-020-02967-7

6. Bebo B, Cintina I, Larocca N, Ritter L, Talente B, Hartung D, Ngorsuraches S, Wallin M, Yang G (2022) The Economic Burden of Multiple Sclerosis in the United States: Estimate of Direct and Indirect Costs. Neurology 98(18):E1810–E1817. https://doi.org/10.1212/WNL.0000000000200150
7. Bekku Y, Rauch U, Ninomiya Y, Oohashi T (2009) Brevican distinctively assembles extracellular components at the large diameter nodes of Ranvier in the CNS. J Neurochem 108(5):1266–1276. https://doi.org/10.1111/J.1471-4159.2009.05873
8. Berek K, Hegen H, Auer M, Barket R, Di Pauli F, Hocher J, Krajnc N, Zinganell A, Deisenhammer F, Berger T, Bsteh G (2024) Odour discrimination and identification as a biomarker of long-term disability worsening in multiple sclerosis. Mult Scler 30(1):55–62. https://doi.org/10.1177/13524585231201093
9. Bijlard M, De Jonge JC, Klunder B, Nomden A, Hoekstra D, Baron W (2016) MAL Is a Regulator of the Recruitment of Myelin Protein PLP to Membrane Microdomains. PLoS ONE 11(5):e0155317. https://doi.org/10.1371/journal.pone.0155317
10. Blanchart A, De Carlos JA, López-Mascaraque L (2006) Time frame of mitral cell development in the mice olfactory bulb. J Comp Neurol 496(4):529–543. https://doi.org/10.1002/cne.20941
11. Booss J, Esiri MM, Tourtellotte WW, Mason DY (1983) Immunohistological analysis of T lymphocyte subsets in the central nervous system in chronic progressive multiple sclerosis. J Neurol Sci 62(1–3):219–232. https://doi.org/10.1016/0022-510X(83)90201-0
12. Boutitah-Benyaich I, Eixarch H, Villacieros-Álvarez J, Hervera A, Cobo-Calvo Á, Montalban X, Espejo C (2025) Multiple sclerosis: molecular pathogenesis and therapeutic intervention. Signal Transduct Target Therapy 10(1). https://doi.org/10.1038/s41392-025-02415-4
13. Brunjes PC, Collins LN, Osterberg SK, Phillips AM (2014) The mouse olfactory peduncle. 3. Development of neurons, glia, and centrifugal afferents. Front Neuroanat 8(JUN). https://doi.org/10.3389/fnana.2014.00044
14. Butt AM, Hornby MF, Ibrahim M, Kirvell S, Graham A, Berry M (1997) PDGF-α Receptor and Myelin Basic Protein mRNAs Are Not Coexpressed by Oligodendrocytesin Vivo:A Doublein SituHybridization Study in the Anterior Medullary Velum of the Neonatal Rat. Mol Cell Neurosci 8(5):311–322. https://doi.org/10.1006/mcne.1996.0590
15. Calver AR, Hall AC, Yu WP, Walsh FS, Heath JK, Betsholtz C, Richardson WD (1998) Oligodendrocyte population dynamics and the role of PDGF in vivo. Neuron 20(5):869–882. https://doi.org/10.1016/S0896-6273(00)80469-9
16. Cecyn MN, Abrahao KP (2023) Where do you measure the Bregma for rodent stereotaxic surgery? IBRO Neurosci Rep 15:143–148. https://doi.org/10.1016/j.ibneur.2023.07.003
17. Collins L, Brunjes P (2020) Experimental Demyelination of the Lateral Olfactory Tract and Anterior Commissure. Neuroscience 434:93–101. https://doi.org/10.1016/j.neuroscience.2020.03.026
18. Concha L, Livy DJ, Beaulieu C, Wheatley BM, Gross DW (2010) In Vivo Diffusion Tensor Imaging and Histopathology of the Fimbria-Fornix in Temporal Lobe Epilepsy. *The Journal of Neuroscience*, *30*(3),

996.
https://doi.org/10.1523
/JNEUROSCI.1619-09.2010 DeLuca, G. C., Joseph, A., George, J., Yates, R. L., Hamard, M., Hofer, M., Esiri, M. M. (2015). Olfactory Pathology in Central Nervous System Demyelinating Diseases. *Brain Pathology (Zurich, Switzerland)*, *25*(5), 543–551. https://doi.org/10.1111/bpa.12209

19. Desai MS, Seekatz AM, Koropatkin NM, Kamada N, Hickey CA, Wolter M, Pudlo NA, Kitamoto S, Terrapon N, Muller A, Young VB, Henrissat B, Wilmes P, Stappenbeck TS, Núñez G, Martens EC (2016) A Dietary Fiber-Deprived Gut Microbiota Degrades the Colonic Mucus Barrier and Enhances Pathogen Susceptibility. *Cell*, *167*(5), 1339–1353.e21. https://doi.org/10.1016/j.cell.2016.10.043 Dogan, E., Gungor, A., Dogulu, F., & Türe, U. (2022). The historical evolution of the fornix and its terminology: a review. *Neurosurgical Review*, *45*(2), 979–988. https://doi.org/10.1007/s10143-021-01635-w
20. Dong Y, Yong VW (2019) When encephalitogenic T cells collaborate with microglia in multiple sclerosis. Nat reviews Neurol 15(12):704–717. https://doi.org/10.1038/s41582-019-0253-6
21. Duncan ID, Radcliff AB (2016) Inherited and acquired disorders of myelin: The underlying myelin pathology. Experimental Neurology 283(Pt B) 452–475. https://doi.org/10.1016/j.expneurol.2016.04.002
22. Emery B (2010) Regulation of oligodendrocyte differentiation and myelination. Sci (New York N Y) 330(6005):779–782. https://doi.org/10.1126/SCIENCE.1190927
23. Frischer JM, Bramow S, Dal-Bianco A, Lucchinetti CF, Rauschka H, Schmidbauer M, Laursen H, Sorensen PS, Lassmann H (2009) The relation between inflammation and neurodegeneration in multiple sclerosis brains. Brain 132(Pt 5):1175–1189. https://doi.org/10.1093/brain/awp070
24. Gabrielli M, Prada I, Joshi P, Falcicchia C, D'Arrigo G, Rutigliano G, Battocchio E, Zenatelli R, Tozzi F, Radeghieri A, Arancio O, Origlia N, Verderio C (2022) Microglial large extracellular vesicles propagate early synaptic dysfunction in Alzheimer's disease. Brain 145(8):2849–2868. https://doi.org/10.1093/brain/awac083
25. Garcia-Gonzalez D, Murcia-Belmonte V, Clemente D, Castro F, De (2013) Olfactory system and demyelination. Anat Record (Hoboken N J : 2007) 296(9):1424–1434. https://doi.org/10.1002/ar.22736
26. Garton T, Gadani SP, Gill AJ, Calabresi PA (2024) Neurodegeneration and demyelination in multiple sclerosis. Neuron 112(19):3231–3251. https://doi.org/10.1016/j.neuron.2024.05.025
27. Ghorbani S, Jelinek E, Jain R, Buehner B, Li C, Lozinski BM, Sarkar S, Kaushik DK, Dong Y, Wight TN, Karimi-Abdolrezaee S, Schenk GJ, Strijbis EM, Geurts J, Zhang P, Ling CC, Yong VW (2022) Versican promotes T helper 17 cytotoxic inflammation and impedes oligodendrocyte precursor cell remyelination. Nat Commun 2022 13:1(1):2445. https://doi.org/10.1038/s41467-022-30032-0. *13*
28. Glezer I, Simard AR, Rivest S (2007) Neuroprotective role of the innate immune system by microglia. Neuroscience 147(4):867–883. https://doi.org/10.1016/j.neuroscience.2007.02.055

29. Green TRF, Rowe RK (2024) Quantifying microglial morphology: an insight into function. Clin Exp Immunol 216(3):221–229. https://doi.org/10.1093/cei/uxae023
30. Hampton SE, Holmes EE, Scheef LP, Scheuerell MD, Katz SL, Pendleton DE, Ward EJ (2013) Quantifying effects of abiotic and biotic drivers on community dynamics with multivariate autoregressive (MAR) models. Ecology 94(12):2663–2669. https://doi.org/10.1890/13-0996.1
31. Harlow DE, Macklin WB (2014) Inhibitors of myelination: ECM changes, CSPGs and PTPs. Exp Neurol 251:39–46. https://doi.org/10.1016/j.expneurol.2013.10.017
32. Hirata T, Fujisawa H (1999) Environmental control of collateral branching and target invasion of mitral cell axons during development. J Neurobiol 38(1):93–104. https://doi.org/10.1002/(SICI)1097-4695::AID-NEU7>3.0.CO;2-N
33. Hiratsuka D, Kurganov E, Furube E, Morita M, Miyata S (2019) VEGF- and PDGF-dependent proliferation of oligodendrocyte progenitor cells in the medulla oblongata after LPC-induced focal demyelination. J Neuroimmunol 332:176–186. https://doi.org/10.1016/j.jneuroim.2019.04.016
34. Höftberger R, Lassmann H (2017) Inflammatory demyelinating diseases of the central nervous system. Handb Clin Neurol 145:263–283. https://doi.org/10.1016/B978-0-12-802395-2.00019-5
35. Irvine KA, Blakemore WF (2008) Remyelination protects axons from demyelination-associated axon degeneration. Brain: J neurology 131(Pt 61464–1477. https://doi.org/10.1093/brain/awn080
36. Kataria H, Alizadeh A, Shahriary GM, Rizi S, Henrie S, Santhosh R, Thliveris KT, J. A., Karimi-Abdolrezaee S (2018) Neuregulin-1 promotes remyelination and fosters a pro-regenerative inflammatory response in focal demyelinating lesions of the spinal cord. Glia 66(3):538–561. https://doi.org/10.1002/glia.23264
37. Kenagy RD, Min SK, Clowes AW, Sandy JD (2009) Cell death-associated ADAMTS4 and versican degradation in vascular tissue. J Histochem Cytochemistry: Official J Histochem Soc 57(9):889–897. https://doi.org/10.1369/jhc.2009.953901
38. Keough MB, Rogers JA, Zhang P, Jensen SK, Stephenson EL, Chen T, Hurlbert MG, Lau LW, Rawji KS, Plemel JR, Koch M, Ling CC, Yong VW (2016) An inhibitor of chondroitin sulfate proteoglycan synthesis promotes central nervous system remyelination. *Nature Communications*, *7*. https://doi.org/10.1038/ncomms11312
39. Kipp M, van der Star B, Vogel DY, Puentes F, van der Valk P, Baker D, Amor S (2012) Experimental in vivo and in vitro models of multiple sclerosis: EAE and beyond. Multiple Scler Relat disorders 1(1):15–28. https://doi.org/10.1016/j.msard.2011.09.002
40. Kraft AD, Harry J (2011) G. Features of Microglia and Neuroinflammation Relevant to Environmental Exposure and Neurotoxicity. *International Journal of Environmental Research and Public Health 2011, Vol. 8, Pages 2980–3018*, *8*(7), 2980–3018. https://doi.org/10.3390/ijerph8072980
41. Lloyd AF, Miron VE (2019) The pro-remyelination properties of microglia in the central nervous system. Nat Reviews Neurol 15(8):447–458. https://doi.org/10.1038/s41582-019-0184-2
42. Lohman AHM, Mentink GM (1969) The lateral olfactory tract, the anterior commissure and the cells of the olfactory bulb. Brain Res 12(2):396–413. https://doi.org/10.1016/0006-8993(69)90008-0

43. López-Muguruza E, Matute C (2023) Alterations of Oligodendrocyte and Myelin Energy Metabolism in Multiple Sclerosis. Int J Mol Sci 24(16). https://doi.org/10.3390/IJMS241612912
44. Mirmosayyeb O, Ebrahimi N, Barzegar M, Afshari-Safavi A, Bagherieh S, Shaygannejad V (2022) Olfactory dysfunction in patients with multiple sclerosis; A systematic review and meta-analysis. PLoS ONE 17(4). https://doi.org/10.1371/journal.pone.0266492
45. Miron VE, Boyd A, Zhao JW, Yuen TJ, Ruckh JM, Shadrach JL, van Wijngaarden P, Wagers AJ, Williams A, Franklin RJM, Ffrench-Constant C (2013) M2 microglia and macrophages drive oligodendrocyte differentiation during CNS remyelination. Nat Neurosci 16(9):1211–1218. https://doi.org/10.1038/nn.3469
46. Molina-Gonzalez I, Miron VE, Antel JP (2022) Chronic oligodendrocyte injury in central nervous system pathologies. Commun Biology 5(1). https://doi.org/10.1038/S42003-022-04248-1
47. Ogawa T, Hagihara K, Suzuki M, Yamaguchi Y (2001) Brevican in the developing hippocampal fimbria: differential expression in myelinating oligodendrocytes and adult astrocytes suggests a dual role for brevican in central nervous system fiber tract development. J Comp Neurol 432(3):285–295. https://doi.org/10.1002/cne.1103
48. Oost W, Meilof JF, Baron W (2025) Multiple sclerosis: what have we learned and can we still learn from electron microscopy. Cell Mol Life Sci 82(1). https://doi.org/10.1007/s00018-025-05690-0
49. Osso LA, Hughes EG (2024) Dynamics of mature myelin. Nat Neurosci 27(8):1449–1461. https://doi.org/10.1038/S41593-024-01642-2
50. Paxinos G, Keith BJ, F (2019) The mouse brain in steteotaxic coordinates. Elsevier Science
51. Peruzzotti-Jametti L, Vicario N, Volpe G, Rizzi S, Kwok C, Lombardi I, Bergholt MS, Barea-Moya L, D'Angelo A, Nicaise AM, D'Amico G, Krzak G, Willis CM, Gil-Perotin S, Hruba O, Braga A, Stevens MM, Garcia-Verdugo JM, Saeb-Parsy K, Pluchino S (2025) Remyelination of chronic demyelinated lesions with directly induced neural stem cells. Brain 148(10):3505–3513. https://doi.org/10.1093/brain/awaf208
52. Plemel JR, Michaels NJ, Weishaupt N, Caprariello AV, Keough MB, Rogers JA, Yukseloglu A, Lim J, Patel VV, Rawji KS, Jensen SK, Teo W, Heyne B, Whitehead SN, Stys PK, Yong VW (2018) Mechanisms of lysophosphatidylcholine-induced demyelination: A primary lipid disrupting myelinopathy. Glia 66(2):327–347. https://doi.org/10.1002/glia.23245
53. Printza A, Boziki M, Valsamidis C, Bakirtzis C, Constantinidis J, Grigoriadis N, Triaridis S (2022) Smell as a Disease Marker in Multiple Sclerosis. J Clin Med 11(17). https://doi.org/10.3390/jcm11175215
54. Redwine JM, Armstrong RC (1998) In vivo proliferation of oligodendrocyte progenitors expressing PDGFalphaR during early remyelination. J Neurobiol 37(3):413–428. https://doi.org/10.1002/(SICI)1097-4695(19981115)37:3%3C413::AID-NEU7%3E3.0.CO;2-8
55. Reich DS, Lucchinetti CF, Calabresi PA (2018) Multiple Sclerosis. N Engl J Med 378(2):169–180. https://doi.org/10.1056/nejmra1401483

56. Rexrode LE, Hartley J, Showmaker KC Molecular profiling of the hippocampus of children with autism spectrum disorder. et al (2024) https://doi.org/10.1038/s41380-024-02441-8Rokach, M., Levy, G., Elad-Sfadia, G., & Barak, B. (2026). Early-Age Cuprizone Exposure Induces Region-Specific Demyelination and Neuroinflammation in Mice. *Neuromolecular Medicine*, *28*(1). https://doi.org/10.1007/s12017-026-08911-2
57. Samtani G, Kim S, Michaud D, Hillhouse AE, Szule JA, Konganti K, Li J (2023) Brain region dependent molecular signatures and myelin repair following chronic demyelination. *Frontiers in Cellular Neuroscience*, *17*. https://doi.org/10.3389/fncel.2023.1169786
58. Schneider CA, Rasband WS, Eliceiri KW (2012) NIH Image to ImageJ: 25 years of image analysis. *Nature Methods*, *9*(7), 671–675. https://doi.org/10.1038/NMETH.2089 Schwabenland, M., Brück, W., Priller, J., Stadelmann, C., Lassmann, H., & Prinz, M. (2021). Analyzing microglial phenotypes across neuropathologies: a practical guide. *Acta neuropathologica*, *142*(6), 923–936. https://doi.org/10.1007/s00401-021-02370-8
59. Schwob JE, Price JL (1984) The development of axonal connections in the central olfactory system of rats. J Comp Neurol 223(2):177–202. https://doi.org/10.1002/cne.902230204
60. Senova S, Fomenko A, Gondard E, Lozano AM (2020) Anatomy and function of the fornix in the context of its potential as a therapeutic target. J Neurol Neurosurg Psychiatry 91(5):547–559. https://doi.org/10.1136/jnnp-2019-322375
61. Serwanski DR, Rasmussen AL, Brunquell CB, Perkins SS, Nishiyama A (2018) Sequential Contribution of Parenchymal and Neural Stem Cell-Derived Oligodendrocyte Precursor Cells toward Remyelination. Neurogl (Basel Switzerland) 1(1):91–105. https://doi.org/10.3390/neuroglia1010008
62. Shigemoto-Mogami Y, Hoshikawa K, Goldman JE, Sekino Y, Sato K (2014) Microglia Enhance Neurogenesis and Oligodendrogenesis in the Early Postnatal Subventricular Zone. J Neurosci 34(6):2231–2243. https://doi.org/10.1523/JNEUROSCI.1619-13.2014
63. Simons M, Nave KA (2015) Oligodendrocytes: Myelination and Axonal Support. Cold Spring Harb Perspect Biol 8(1). https://doi.org/10.1101/cshperspect.a020479
64. Soussi-Yanicostas N, De Castro F, Julliard AK, Perfettini I, Chédotal A, Petit C (2002) Anosmin-1, defective in the X-linked form of Kallmann syndrome, promotes axonal branch formation from olfactory bulb output neurons. Cell 109(2):217–228. https://doi.org/10.1016/S0092-8674(02)00713-4
65. Steelman AJ, Thompson JP, Li J (2012) Demyelination and remyelination in anatomically distinct regions of the corpus callosum following cuprizone intoxication. Neurosci Res 72(1):32–42. https://doi.org/10.1016/j.neures.2011.10.002
66. Stidworthy MF, Genoud S, Suter U, Mantei N, Franklin RJM (2006) Quantifying the Early Stages of Remyelination Following Cuprizone-induced Demyelination. Brain Pathol 13(3):329. https://doi.org/10.1111/j.1750-3639.2003.tb00032
67. Tafti D, Ehsan M, Xixis KL (2026) Multiple Sclerosis. *StatPearls*. https://pubmed.ncbi.nlm.nih.gov/29763024/

68. Tranel D, Welsh-Bohmer KA (2012) Pervasive olfactory impairment after bilateral limbic system destruction. J Clin Exp Neuropsychol 34(2):117–125. https://doi.org/10.1080/13803395.2011.633897
69. Vanderdonckt P, Aloisi F, Comi G, De Bruyn A, Hartung HP, Huitinga I, Kuhlmann T, Lucchinetti CF, Metz I, Reynolds R, Lassmann H (2022) Tissue donations for multiple sclerosis research: current state and suggestions for improvement. Brain Commun 4(2). https://doi.org/10.1093/braincomms/fcac094
70. Vereyken EJF, Fluitsma DM, Bolijn MJ, Dijkstra CD, Teunissen CE (2009) An in vitro model for de- and remyelination using lysophosphatidyl choline in rodent whole brain spheroid cultures. Glia 57(12):1326–1340. https://doi.org/10.1002/glia.20852
71. Wyss JM, Swanson LW, Cowan WM (1980) The organization of the fimbria, dorsal fornix and ventral hippocampal commissure in the rat. Anat Embryol 158(3):303–316. https://doi.org/10.1007/BF00301819
72. Yamazaki R, Ohno N, Huang JK (2021) Acute motor deficit and subsequent remyelination-associated recovery following internal capsule demyelination in mice. J Neurochem 156(6):917–928. https://doi.org/10.1111/jnc.15142
73. Yamazaki R, Osanai Y, Kouki T, Huang JK, Ohno N (2023) Pharmacological treatment promoting remyelination enhances motor function after internal capsule demyelination in mice. Neurochem Int 164:105505. https://doi.org/10.1016/j.neuint.2023.105505
74. Young KM, Psachoulia K, Tripathi RB, Dunn SJ, Cossell L, Attwell D, Tohyama K, Richardson WD (2013) Oligodendrocyte dynamics in the healthy adult CNS: Evidence for myelin remodeling. Neuron 77(5):873–885. https://doi.org/10.1016/j.neuron.2013.01.006
75. Zheng K, Wang C, Yang J, Huang H, Zhao X, Zhang Z, Qiu M (2018) Molecular and Genetic Evidence for the PDGFRα-Independent Population of Oligodendrocyte Progenitor Cells in the Developing Mouse Brain. J Neuroscience: Official J Soc Neurosci 38(44):9505–9513. https://doi.org/10.1523/JNEUROSCI.1510-18.2018
76. Zhu Q, Zhao X, Zheng K, Li H, Huang H, Zhang Z, Mastracci T, Wegner M, Chen Y, Sussel L, Qiu M (2014a) Genetic evidence that Nkx2.2 and Pdgfra are major determinants of the timing of oligodendrocyte differentiation in the developing CNS. Development 141(3):548–555. https://doi.org/10.1242/dev.095323

Figures

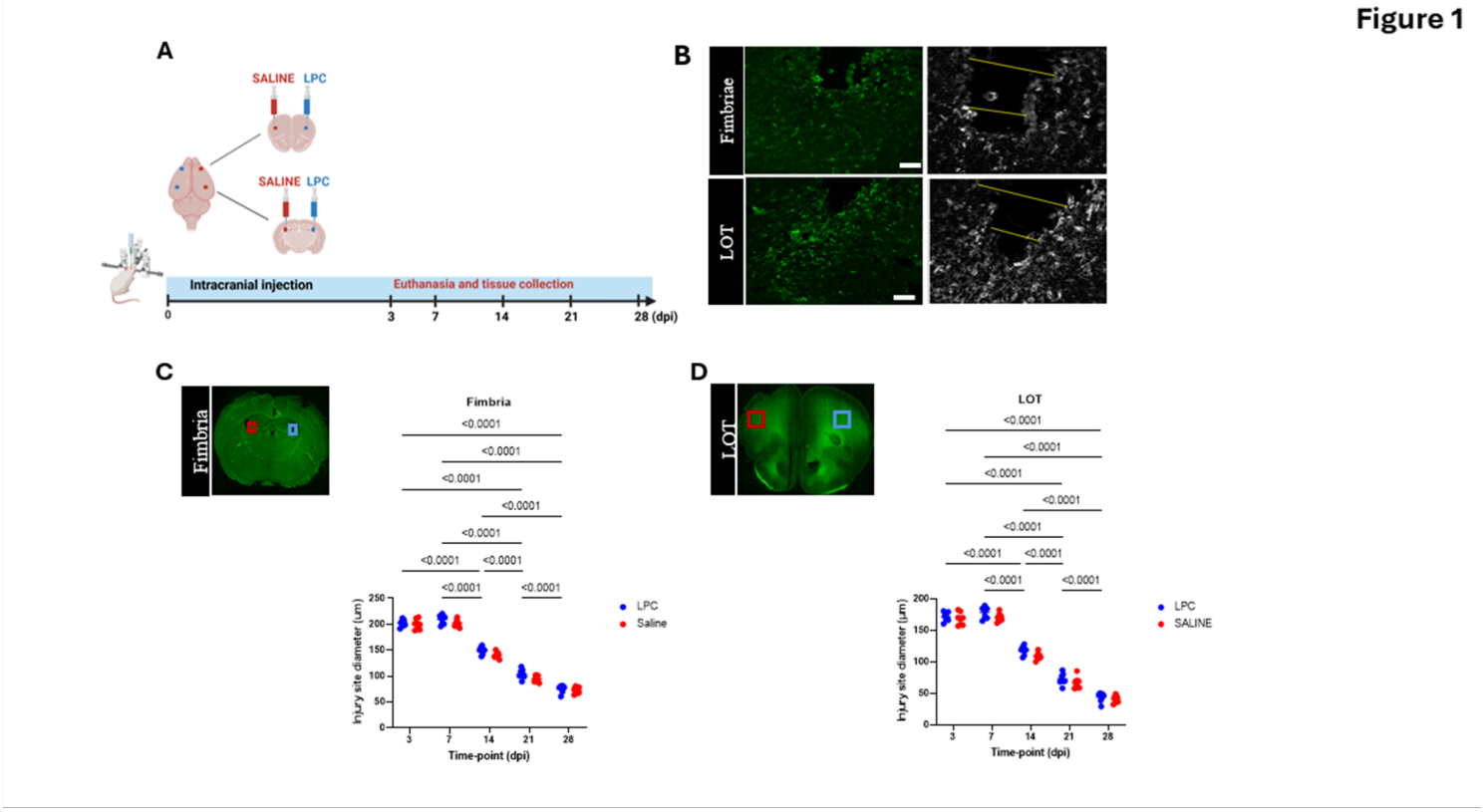


Figure 1

Lysophosphatidylcholine (LPC)-induced demyelination of the hippocampal fimbria (HPF) and lateral olfactory tract (LOT). (**A**) Timeline indicating the experimental design and intracranial injection of LPC (ipsilateral hemisphere) and saline (contralateral hemisphere)in the HPF and LOT and subsequent euthanasia and analysis at 3, 7-, 14-, 21- and 28 days post-injection (dpi). (**B**) Representative images for IBA immunofluorescent staining showing lesion site in the fimbria and LOT following the injection of LPC. Scale bar, 20 µm. Yellow line indicates the lesion diameter. Data analysis of lesion diameter in the (**C**) fimbria and (**D**) LOT regions at different time points (3-28 dpi). Data is presented as mean ± SD, and statistical analysis was conducted using two-way mixed-effects ANOVA by Tukey's multiple comparisons test (n = 20). The red and blue squares show injection site in the ipsilateral and contralateral hemisphere, respectively.

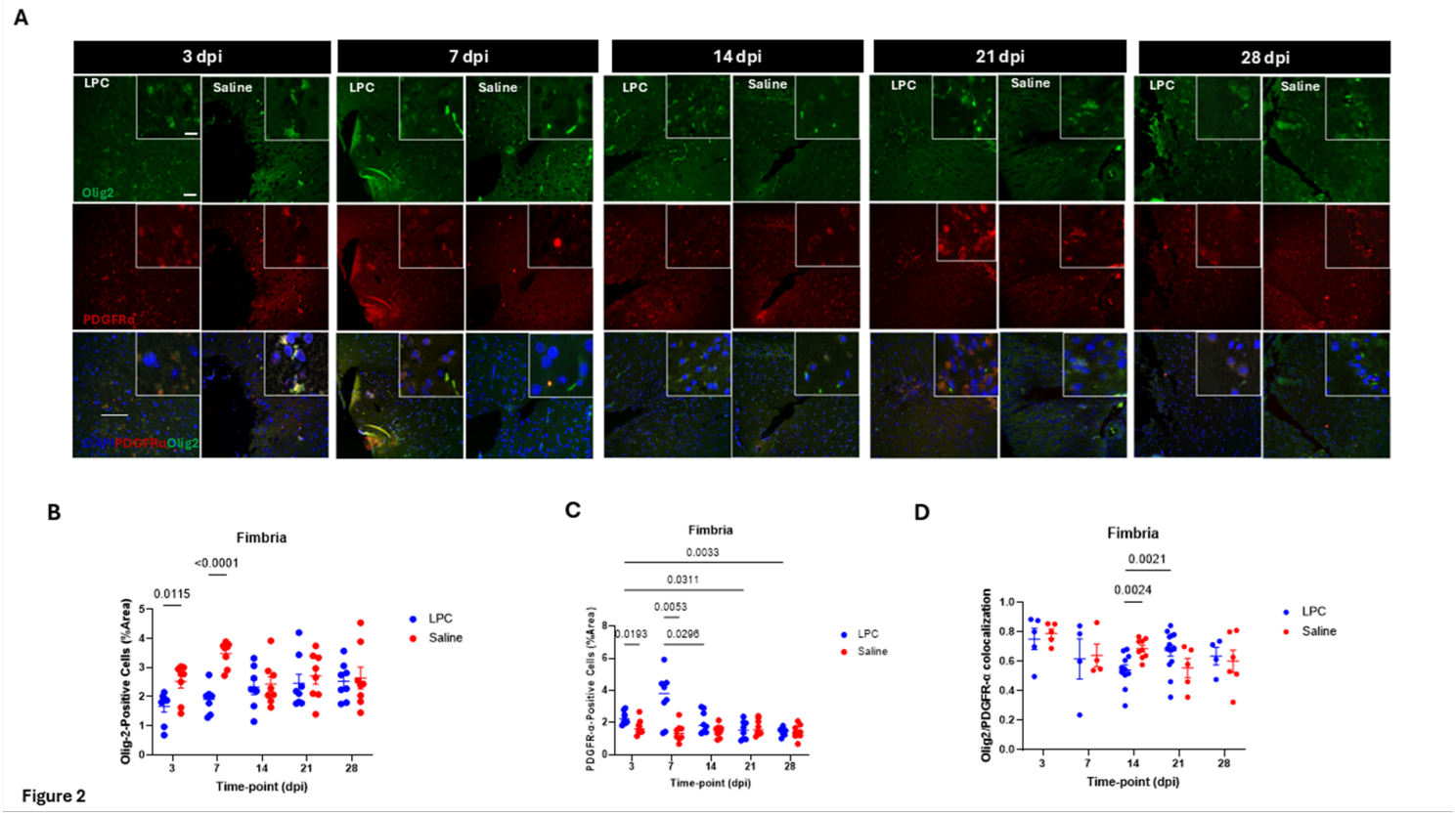


Figure 2

Figure 2

Oligodendrocyte precursor cell recruitment and Olig2 lineage progression in fimbrial lesion site (**A**) Representative images of Olig2 (green) and PDGFRα (red) double immunofluorescence staining in the fimbria at 3, 7, 14, 21, and 28 days post-injury (dpi) following injection of LPC and saline Scale bar: 50 µm. The white square inset images show a higher magnification of the region surrounding the injection sites. Scale bar: 20 µm. Quantification of (**B**) Olig2⁺ cells, (**C**) PDGFRα⁺ cells, and (**D**) Olig2⁺ and PDGFRα⁺ co-localized cells within the lesion site in the fimbria across different time points (3-28 dpi). Data is presented as mean ± SD. Statistical analysis was performed using two-way mixed-effects ANOVA followed by Tukey's multiple comparisons test to assess differences across time points and within the lesion site. (n=20). Exact *p* values are indicated in the graphs.

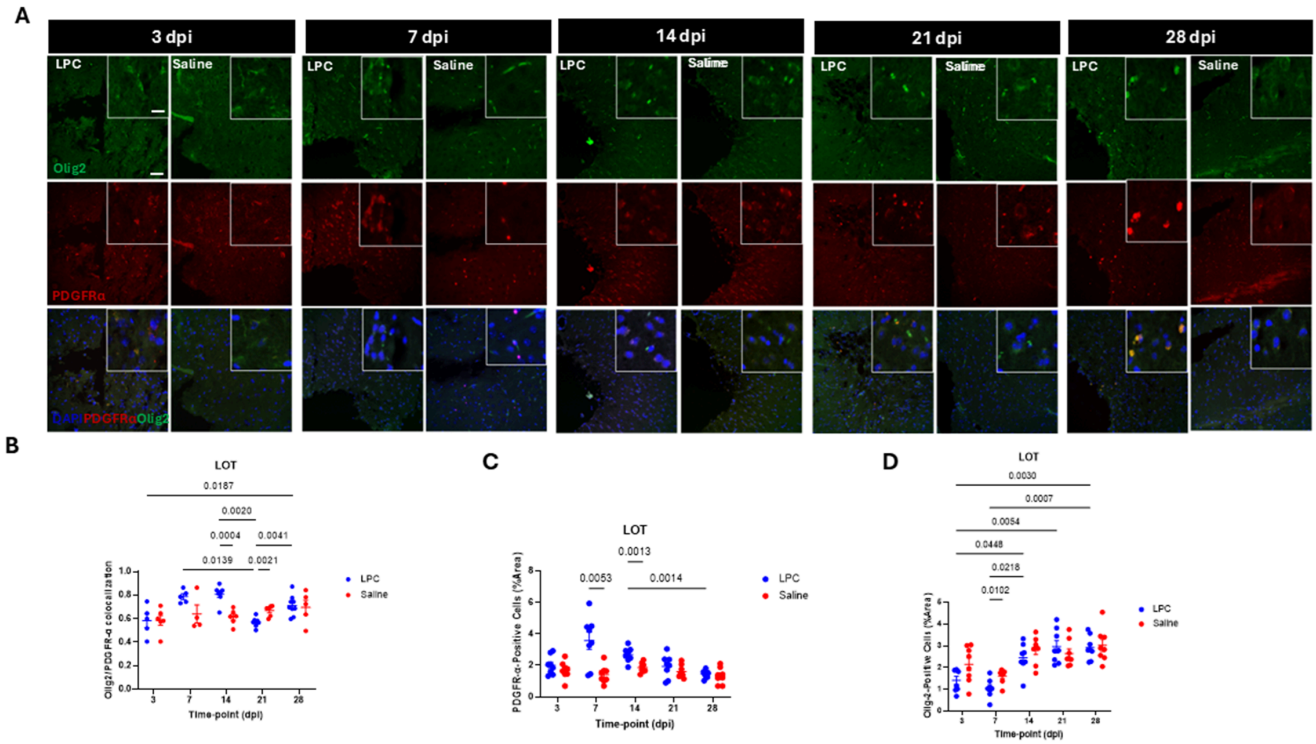


Figure 3

Figure 3

Oligodendrocyte precursor cell recruitment and Olig2 lineage progression in the lateral olfactory tract (LOT) lesion site (**A**) Representative images of Olig2 (green) and PDGFRα (red) double immunofluorescence staining in the LOT during the post-injury time course (3-28 dpi) following injection of LPC and saline. Scale bar: 50 μm. The white square inset images show a higher magnification of the region surrounding the injection sites. Scale bar: 20 μm. Quantification of (**B**) Olig2⁺ cells, (**C**) PDGFRα⁺ cells, and (**D**) Olig2⁺ and PDGFRα⁺ co-localized cells within the lesion site in the LOT across different time points (3-28 dpi). Data is presented as mean ± SD. Statistical analysis was performed using two-way mixed-effects ANOVA followed by Tukey's multiple comparisons test to assess differences across time points and within the lesion site. Exact *p* values are indicated in the graphs.

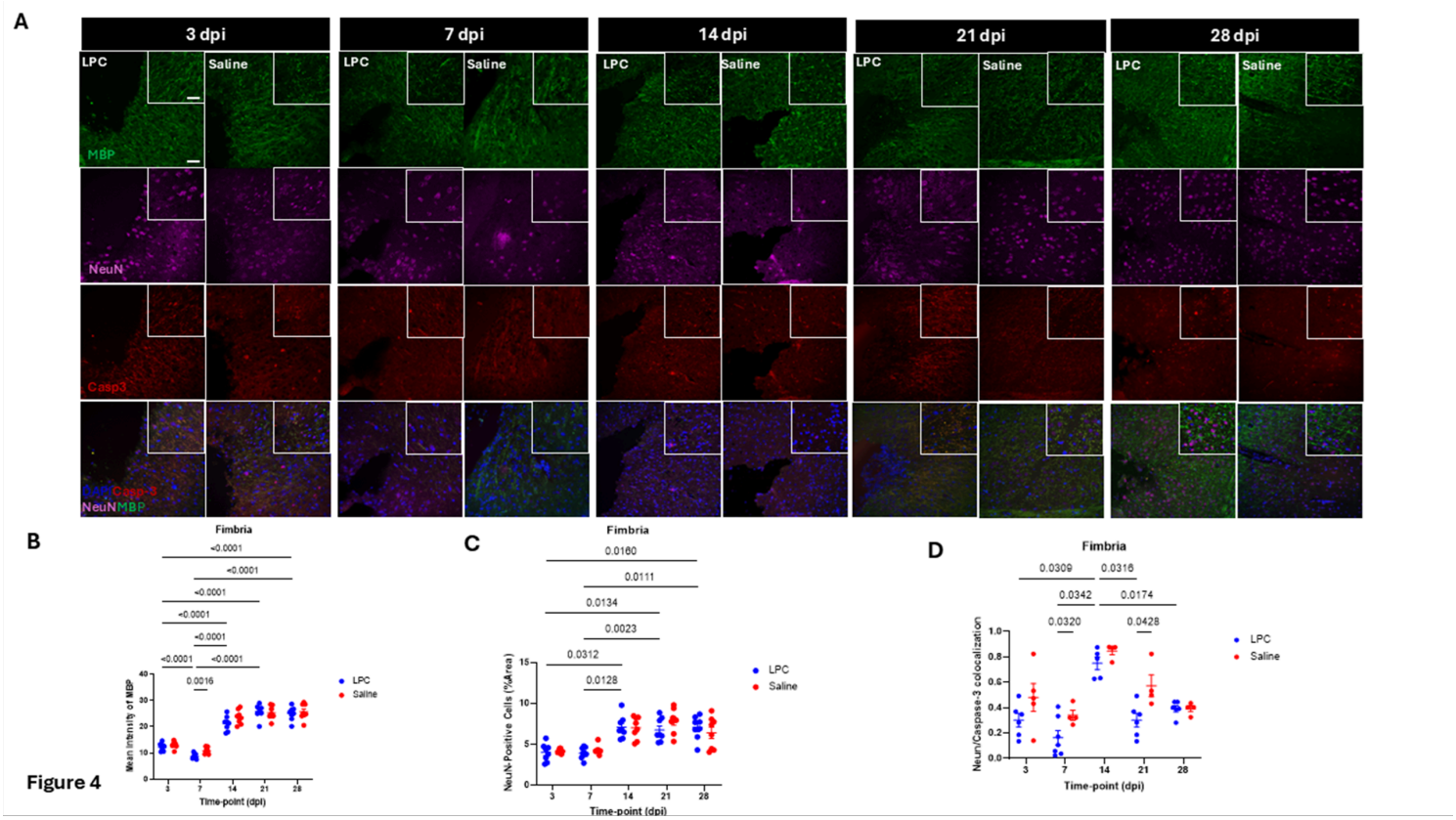


Figure 4

Extent of demyelination, neuronal density and apoptosis at the fimbrial lesion site (**A**) Representative immunofluorescence images showing MBP (green), NeuN (magenta), and Caspase-3 (red) expression in the fimbria at 3, 7, 14, 21, and 28 days post-injury (dpi), scale bar = 50 µm. The white square inset images show a higher magnification of the region surrounding the injection sites. Scale bar: 20 µm. Quantification of (**B**) Myelin basic protein MBP intensity, (**C**) NeuN and (**D**) Caspase-3 and NeuN colocalization in the fimbrial lesion site across different time points (3-28 dpi). Data is presented as mean ± SD. Statistical analysis was performed using two-way mixed-effects ANOVA followed by Tukey's multiple comparisons test to assess differences across time points and within the lesion site (n = 20). Exact *p* values are indicated in the graphs.

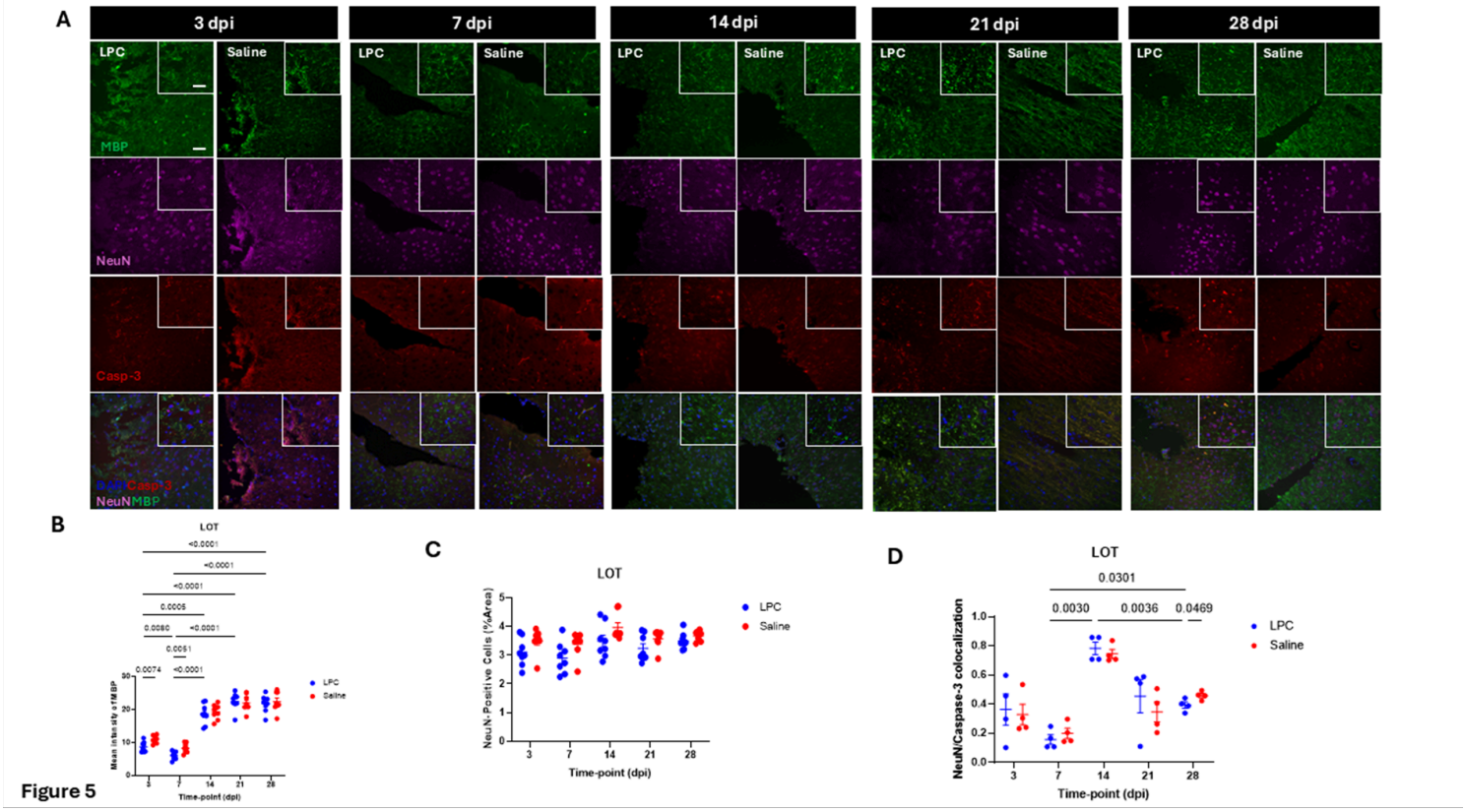


Figure 5

Figure 5

Extent of demyelination, neuronal density and apoptosis at the lateral olfactory tract (LOT) lesion site (**A**) Representative immunofluorescence images showing MBP (green), NeuN (magenta), and Caspase-3 (red) expression in the LOTat 3, 7, 14, 21, and 28 days post-injury (dpi), scale bar = 50 µm. The white square inset images show a higher magnification of the region surrounding the injection sites. Scale bar: 20 µm. Quantification of (**B**) Myelin basic protein MBP intensity, (**C**) NeuN and (**D**) Caspase-3 and NeuN colocalization within the LOT lesion site across different time points (3-28 dpi). Data is presented as mean ± SD. Statistical analysis was performed using two-way mixed-effects ANOVA followed by Tukey's multiple comparisons test to assess differences across time points and within the lesion site (n = 20). Exact *p* values are indicated in the graphs.

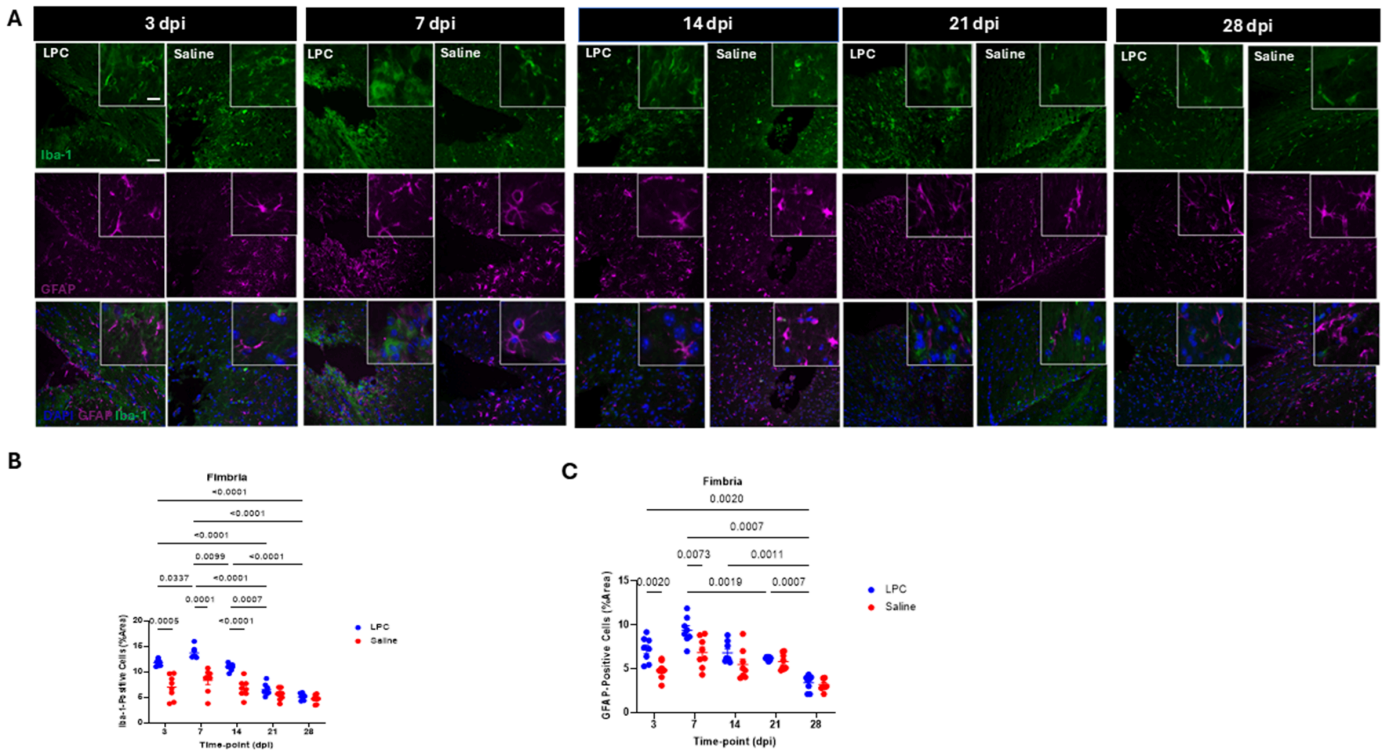


Figure 6

Figure 6

Astrocyte and microglial response at the fimbrial lesion site (**A**) Representative immunofluorescence images showing microglial (green) and astrocyte (magenta) accumulation at the lesion site in the fimbria at 3, 7, 14, 21, and 28 days post-injury (dpi). Scale bar: 50 µm. The white square inset images show a higher magnification of the region surrounding the injection sites. Scale bar: 20 µm. (**B**) Quantification of IBA-1 positive microglial and (**C**) GFAP positive astrocytes in the fimbria across different time points (3-28 dpi). Data is presented as mean ± SD. Statistical analysis was performed using two-way mixed-effects ANOVA followed by Tukey's multiple comparisons test to assess differences across time points and within the lesion site (n=20). Exact *p*values are indicated in the graphs.

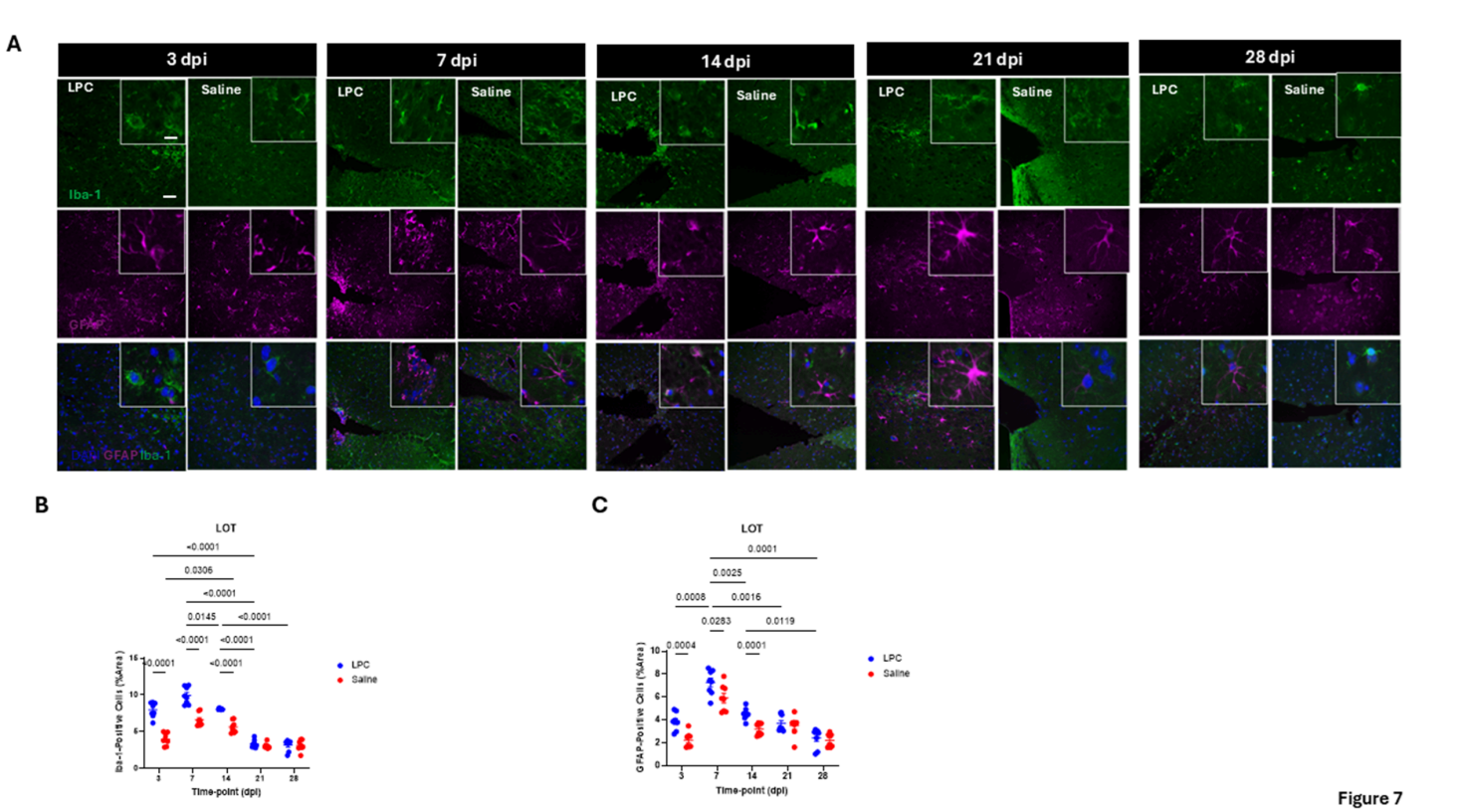


Figure 7

Figure 7

Astrocyte and microglial response at the lateral olfactory tract (LOT) lesion site (**A**) Representative immunofluorescence images showing microglial (green) and astrocyte (magenta) accumulation at the LOT at 3, 7, 14, 21, and 28 days post-injury (dpi). Scale bar: 50 µm. The white square inset images show a higher magnification of the region surrounding the injection sites. Scale bar: 20 µm. (**B**) Quantification of IBA-1 positive microglial and (**C**) GFAP positive astrocytes in the LOT across different time points (3-28 dpi). Data is presented as mean ± SD. Statistical analysis was performed using two-way mixed-effects ANOVA followed by Tukey's multiple comparisons test to assess differences across time points and within the lesion site (n=20). Exact *p*values are indicated in the graphs.

Supplementary Files

This is a list of supplementary files associated with this preprint. Click to download.

- Table1.docx
- Additionalfigure3.tif
- Additionalfigure1.tif
- AdditionalFigure2.tif
- GraphicalAbstract.tif